



## **Geophysical Research Letters**\*



#### **RESEARCH LETTER**

10.1029/2023GL103151

#### **Key Points:**

- Correlation between Newell coupling function (NCF) and total field-aligned current (FAC) is studied for different storm drivers
- Best correlation for sheath, high-speed stream, and magnetic cloud storms is found by integrating NCF over 80, 90, and 140 min, respectively
- Sheath-driven storms are associated with the highest values of total FAC and NCF

#### **Supporting Information:**

Supporting Information may be found in the online version of this article.

#### Correspondence to:

M. N. Pedersen, marcus.pedersen@oulu.fi

#### Citation:

Pedersen, M. N., Vanhamäki, H., & Aikio, A. T. (2023). Comparison of field-aligned current responses to HSS/SIR, sheath, and magnetic cloud driven geomagnetic storms. *Geophysical Research Letters*, 50, e2023GL103151. https://doi.org/10.1029/2023GL103151

Received 8 FEB 2023 Accepted 13 MAY 2023

# © 2023. The Authors. This is an open access article under the terms of the Creative Commons Attribution License, which permits use, distribution and reproduction in any medium, provided the original work is properly cited.

### Comparison of Field-Aligned Current Responses to HSS/SIR, Sheath, and Magnetic Cloud Driven Geomagnetic Storms

M. N. Pedersen<sup>1</sup>, H. Vanhamäki<sup>1</sup>, and A. T. Aikio<sup>1</sup>

<sup>1</sup>Space Physics and Astronomy Research Unit, University of Oulu, Oulu, Finland

**Abstract** The time delay from an interplanetary driver arriving at the magnetopause to the response in the ionosphere has never been quantified separately for different types of storm drivers. This study investigates the delay for storms driven by high-speed streams and associated stream interaction regions (HSS/SIR), or by interplanetary coronal mass ejection sheaths and magnetic clouds (MC). The total field-aligned current (FAC) and SME index lag the Newell coupling function (NCF) by  $40 \pm 10$  min during storms driven by HSS/SIR and sheaths, and by  $60 \pm 10$  min for MCs. The correlation coefficient between FAC and NCF reaches maximum value as NCF is averaged over the preceding 80 min for sheath, 90 min for HSS/SIR, and 140 min for MC storms.

**Plain Language Summary** The Sun causes perturbations in the solar wind, which may drive geomagnetic storms associated with strong field-aligned currents to the ionosphere. The solar wind drivers studied in this paper are high-speed stream/stream interaction regions (HSS/SIR), and sheath and magnetic cloud (MC) interplanetary coronal mass ejections. The exact time from the arrival of the solar wind interplanetary driver at the magnetopause to the response in the ionospheric and field-aligned currents (FAC) have not been quantified for different types of solar wind drivers. We study this time delay during geomagnetic storms and find that it is typically 40 min for HSS/SIR- and sheath-driven storms, and 60 min for MC-driven storms. Additionally, the total FAC best correlate with the solar wind averaged over the preceding 80 min for sheath, 90 min for HSS/SIR, and 140 min for MC-driven storms. These results may help improve the accuracy of forecasting solar wind disturbances on the high-latitude ionosphere.

#### 1. Introduction

The time delay between the solar wind arrival at the magnetopause and the responses throughout the magnetosphere and in the ionosphere has been estimated to range between 10 and 180 min (e.g., Gonzalez et al., 1989; Meng et al., 1973; Rostoker et al., 1972; Wilcox et al., 1967). Different solar wind drivers, and the present state of the magnetosphere and ionosphere all play important roles in the length of the time delay, which makes it difficult to accurately predict (e.g., Maggiolo et al., 2017). It would be of crucial importance to the scientific community to be able to accurately predict the impact of the solar wind on the ionosphere to better mitigate hazardous space weather events and to understand the dynamics and behavior of the ionosphere to solar wind driving. Early studies by Meng et al. (1973) found that the correlation between the auroral electrojet (AE) index and the southward-directed component of the interplanetary magnetic field (IMF) peaked when the interplanetary data was shifted approximately 40 min. McPherron et al. (2018) studied the time lag between the solar wind coupling and the field-aligned currents (FAC) or AE index during substorm events. They found lags of 30–45 min, with the nightside having a larger delay than the dayside. Anderson et al. (2014) reported that the dayside currents appeared within 20 min after a southward turning of the IMF, and that the nightside currents occurred 40–70 min after the dayside currents.

Our previous studies have characterized the typical evolution of FACs, ionospheric equivalent currents, and substorms during high-speed stream/stream interaction region (HSS/SIR) driven storms, as well as storms driven by sheath and magnetic cloud (MC) regions of interplanetary coronal mass ejections (ICME) (Pedersen et al., 2021, 2022). In this paper, we analyze the time delay between the interplanetary driver at the magnetopause and the FACs, ionospheric currents, as well as several geomagnetic indices for the three types of storm drivers using cross-correlation analysis. The integration time of the solar wind driver that produces peak correlation between the Newell coupling function (NCF) and integrated FAC was also estimated. Newell et al. (2007) found that the NCF gives the best correlation with magnetic indices. By using the obtained integration times, the relationship between FAC and the NCF is studied for the three drivers.

PEDERSEN ET AL. 1 of 9

#### 2. Data Analysis Methods

#### 2.1. Data Processing

Active Magnetosphere and Planetary Electrodynamics Response Experiment (AMPERE) provides FAC measurements in the northern and southern hemispheres above 40° magnetic latitude (MLAT) at 2 min cadence over a 10 min window (Anderson et al., 2000, 2002; Waters et al., 2001, 2020). This study focuses on the total integrated downward FAC (equal to the total upward FAC, see Pedersen et al., 2022) in the northern hemisphere during the years 2010–2017 with 10 min time resolution to ensure that the FAC estimates from AMPERE are independent. The integration was done similarly as explained in Pedersen et al. (2021). The solar wind and IMF data from OMNI were processed from 5 min resolution into 10 min averages taken during the same time interval as the FAC. The SuperMAG electrojet index SME and SYM-H index, which each had 1 min time resolution, were processed into 10 min averages in the same way. It is important that the data coincide precisely in time, so that there is no artificial time lag included.

We use the same definitions for storm main phase as in our previous paper (Pedersen et al., 2022), namely the storm main phase onset  $t_0$  began when the SYM-H index decreased to less than -15 nT, and the end of the storm main phase was set to the time the SYM-H index reached a minimum of at least -50 nT. A list of the storms included in this study is in the Supporting Information S1 (28 HSS/SIR, 26 sheath, and 19 MC). The same storms were studied by Pedersen et al. (2021, 2022).

#### 2.2. Cross-Correlation and Time Lag

To estimate the cross-correlation between the parameters, the Pearson correlation coefficient (CC) was calculated for each lag by shifting the time series with steps equivalent to the basic resolution used (10 min). The cross correlation was estimated as:

$$R_{XY}(\Delta t) = \begin{cases} \rho(X(t + \Delta t), Y(t)) & \text{for } \Delta t \ge 0\\ \rho(X(t), Y(t - \Delta t)) & \text{for } \Delta t < 0 \end{cases}$$
 (1)

where  $\rho$  is the Pearson CC, X and Y are the time series of the two parameters, t is [-12 hr, 36 hr] around the main phase onset  $t_0$  and  $\Delta t = 0, \pm 10 \text{ min}, \pm 20 \text{ min}, \dots, \pm 500 \text{ min}$ . Cross-correlation was calculated separately for each storm and the lag  $\Delta t$  yielding the largest  $R_{XY}(\Delta t)$  was labeled the best lag. The reason for shifting both time series in the manner of Equation 1 was to not include any data earlier than 12 hr before the main phase onset.

#### 3. Results

#### 3.1. Autocorrelation Functions

Before looking at cross-correlations, we study the autocorrelation functions (ACF) of selected parameters for the three drivers. Performing the cross-correlation in Equation 1 for a parameter with respect to itself yields the ACF. Figure 1 shows the ACF in all storms (thin lines) and the median (thick line) for NCF (top), FAC (middle) and SME index (bottom) during HSS/SIR (left), sheath (middle) and MC (right)-driven storms. The full width at half maximum (FWHM) value is shown with a vertical dashed line in each panel. The FWHMs of the ACF for the NCF are significantly shorter for HSS/SIR storms (50 min) compared to sheath (165 min) and MC (300 min) storms. This shows that the solar wind-magnetosphere coupling remains stable for shorter time during HSS/SIR storms than in ICME storms. The FWHM values of the drivers are also in the same order as the average storm main phase durations, which are 6, 9, and 12 hr for HSS/SIR, sheath, and MC storms, respectively (Pedersen et al., 2021, 2022). For FACs and SMEs, the widths of ACFs are ordered in the same way as for the corresponding drivers, but the lengths are typically larger. Interestingly, the FWHM values are larger for FAC than for SME.

High-speed solar wind emanating from coronal holes is characterized by large-amplitude outward propagating Alfvén wave trains (Tsurutani et al., 2006; Tsurutani & Gonzalez, 1987; Tsurutani & Ho, 1999). During Alfvén waves, the direction of the IMF varies, while the magnitude, plasma density and pressure stay fairly constant

PEDERSEN ET AL. 2 of 9

19448007, 2023, 11, Downloaded from https://agupubs.onlinelibrary.wiley.com/doi/10.1029/2023GL/103151 by Johns Hopkins University, Wiley Online Library on [1606/2023]. See the Terms and Conditions (https://onlinelibrary.wiley.com/terms/

and-conditions) on Wiley Online Library for rules of use; OA articles are governed by the applicable Cres

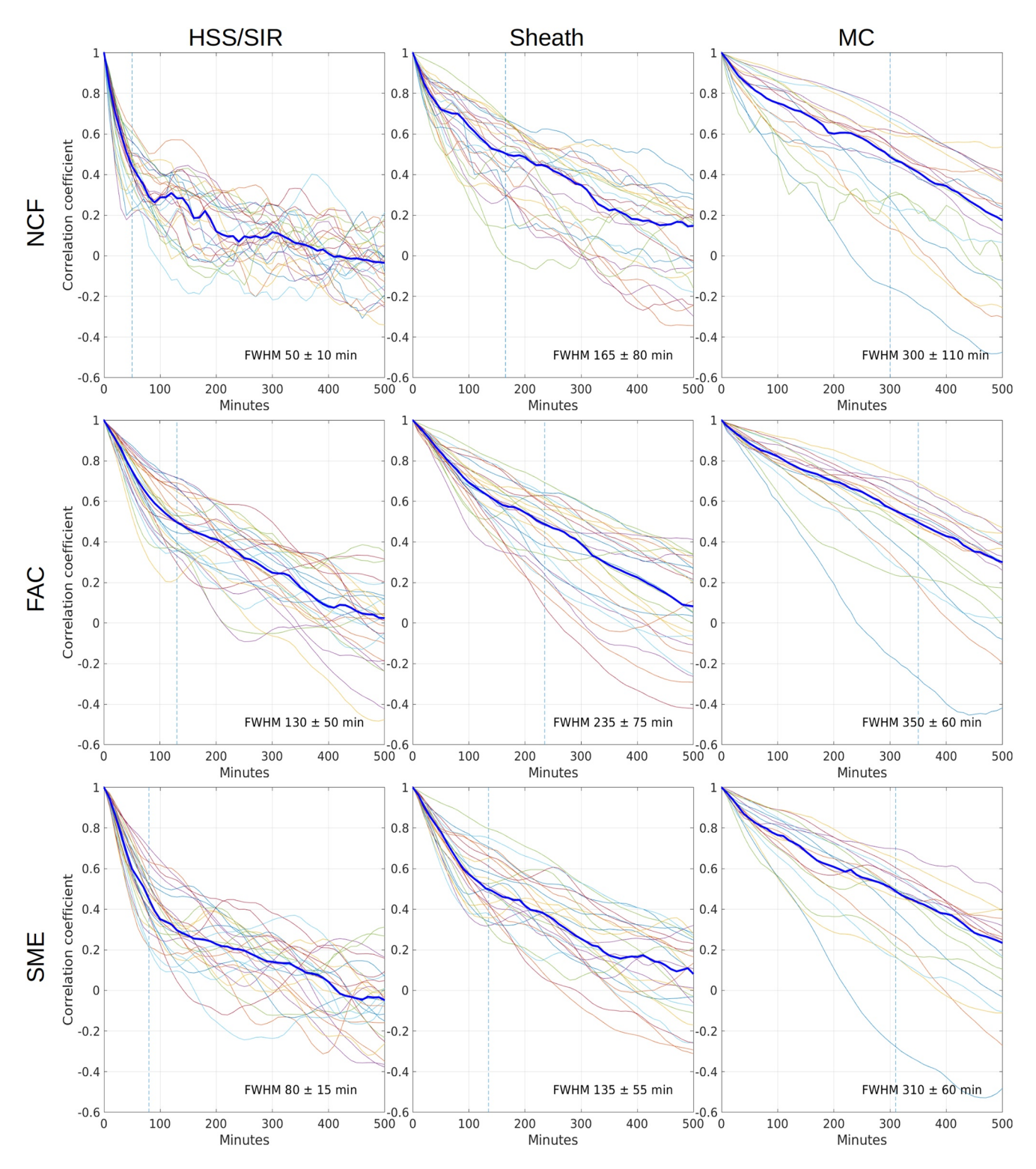
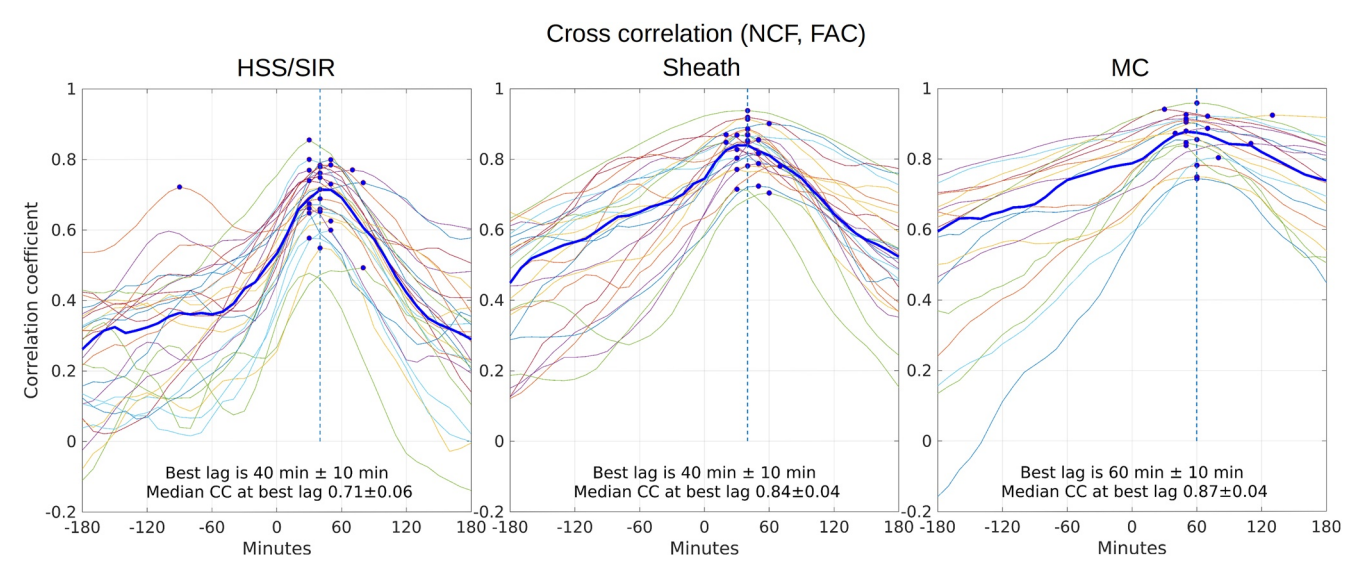


Figure 1. Autocorrelation functions for Newell coupling function (top panels), field-aligned current (middle panels), and SME index (bottom panels) for the high speed streams and associated stream interaction regions (left), sheath (middle), and magnetic cloud (right) storms. The  $\pm$  shows the median absolute deviation from all events in the group.

PEDERSEN ET AL. 3 of 9

19448007, 2023, 11, Downloaded from https://agupubs.onlinelibrary.wiley.com/doi/10.1029/2023GL103151 by Johns Hopkins University, Wiley Online Library on [16/06/2023]. See the



**Figure 2.** Cross-correlation of Newell coupling function and field-aligned current for all high-speed streams and associated stream interaction regions (left), sheath (middle), and magnetic cloud (right) storms. The maximum correlations for each storm are shown with blue circles. The blue bold line shows the median correlation from all storms at each lag. Median of the maximum correlations, that is, the best lag, is shown by a vertical dashed line. The best lag and the median correlation coefficient at the best lag are given in the bottom of panels with median absolute deviations.

(Echer et al., 2011). The IMF fluctuations are correlated with fluctuations in the solar wind velocity and have a broad wavelength range (Belcher & Davis, 1971). The oscillations in Figure 1 are visible in individual events when looking at the ACF for the NCF (Figure 1 top-left corner), and even more visible in the ACF of the IMF  $B_Z$  component for HSS/SIR storms (not shown). This suggests that the short FWHM during HSS/SIR storms for the NCF can be caused by Alfvénic fluctuations. Oscillations are also visible in the FAC and SME of HSS/SIR storms, but to a lesser extent, which shows how the magnetosphere-ionosphere system acts like a low-pass filter.

#### 3.2. Cross-Correlations and Time Lags

Figure 2 shows the cross-correlation between the NCF and FAC for all the HSS/SIR, sheath and MC-driven storms. The bold blue line shows the median of CCs calculated for each lag. In the following discussion, the median of lag values from all the individual storms (solid circles) is called the *best lag* and is marked with a dashed vertical line in Figure 2. The median CC at the best lag can be found from the intersection between the bold blue line and the dashed vertical line. Table 1 reports the best lags in the three categories. The best lag is 40 min for HSS/SIR and sheath storms, and 60 min for MC storms.

The median CC at best lag is 0.71 for HSS/SIR, while for ICME sheath and MC storms it is as high as 0.84 and 0.87, respectively. This is in agreement with Pedersen et al. (2021) and Pedersen et al. (2022) where the unshifted and superposed solar wind coupling functions have higher CCs with FAC and AE index for ICME-driven storms compared to HSS/SIR-driven storms. The cross-correlation peak between the NCF and FAC is sharpest for HSS/SIR storms and flatter for sheath and MC storms, which is likely to be due to the driver, since the auto-correlation for the NCF behaved in the same manner in Figure 1 for the different storms.

One HSS/SIR storm has the maximum CC at a lag of -90 min with CC 0.72. This storm has a second peak at 50 min lag with CC 0.71, in line with the other HSS/SIR storms. The reason for the negative lag is likely the strong periodicity seen in this and some other HSS/SIR storms, possibly caused by strong Alfvénic fluctuations in the high speed solar wind (see e.g., Tsurutani et al., 2006; Tsurutani & Gonzalez, 1987; Tsurutani & Ho, 1999).

Table 1 shows the best lag and corresponding CC together with median absolute deviation (MAD) between several magnetospheric and ionospheric parameters. The FAC and SME/L/U indices are highly correlated with CC of 0.78–0.92 and have best lag at zero, as is expected as both are measured in the ionosphere and are current-related parameters. Delays between the SME/L/U indices and NCF have similar values as for the FAC and NCF. NCF produces generally better CCs than Akasofu  $\varepsilon$ , but delays are about the same. Highest CC values are typically

PEDERSEN ET AL. 4 of 9

**Table 1**Peak Cross-Correlation Coefficients and Corresponding Time Lags With Median Absolute Deviations for Selected Parameters at 10 min Resolution

	Correlation coefficients			Time lag (min)		
Parameters	HSS/SIR	Sheath	MC	HSS/SIR	Sheath	MC
NCF, FAC	0.71 ± 0.09	$0.84 \pm 0.04$	$0.87 \pm 0.04$	40 ± 10	40 ± 10	$60 \pm 10$
NCF, SME	$0.71 \pm 0.05$	$0.82 \pm 0.05$	$0.84 \pm 0.05$	$40 \pm 10$	$35 \pm 15$	$50 \pm 10$
NCF, -SML	$0.65 \pm 0.07$	$0.78 \pm 0.05$	$0.80 \pm 0.04$	$30 \pm 10$	$40 \pm 10$	$60 \pm 20$
NCF, SMU	$0.60 \pm 0.09$	$0.71 \pm 0.11$	$0.76 \pm 0.04$	$30 \pm 10$	$30 \pm 20$	$60 \pm 20$
NCF, PCN	$0.66 \pm 0.07$	$0.75 \pm 0.07$	$0.82 \pm 0.08$	$20 \pm 0$	$20 \pm 10$	$30 \pm 10$
$\varepsilon$ , FAC	$0.72 \pm 0.05$	$0.76 \pm 0.05$	$0.85 \pm 0.02$	$40 \pm 10$	$40 \pm 10$	$70 \pm 10$
$\varepsilon$ , SME	$0.61 \pm 0.08$	$0.73 \pm 0.09$	$0.85 \pm 0.06$	$30 \pm 10$	$35 \pm 15$	$60 \pm 10$
$\varepsilon$ , -SML	$0.56 \pm 0.09$	$0.70 \pm 0.09$	$0.83 \pm 0.07$	$35 \pm 5$	$30 \pm 20$	$60 \pm 20$
$\varepsilon$ , SMU	$0.56 \pm 0.08$	$0.62 \pm 0.09$	$0.72 \pm 0.05$	$40 \pm 20$	$30 \pm 45$	$60 \pm 20$
$\varepsilon$ , PCN	$0.62 \pm 0.06$	$0.66 \pm 0.09$	$0.76 \pm 0.08$	$20 \pm 10$	$20 \pm 20$	$50 \pm 30$
FAC, SME	$0.86 \pm 0.04$	$0.91 \pm 0.03$	$0.92 \pm 0.03$	$0 \pm 0$	$0 \pm 0$	$0 \pm 0$
FAC, -SML	$0.79 \pm 0.06$	$0.88 \pm 0.05$	$0.88 \pm 0.04$	$0 \pm 0$	$0 \pm 0$	$0 \pm 0$
FAC, SMU	$0.78 \pm 0.06$	$0.85 \pm 0.04$	$0.84 \pm 0.03$	$0 \pm 0$	$0 \pm 0$	$0 \pm 10$
FAC, PCN	$0.79 \pm 0.06$	$0.83 \pm 0.04$	$0.83 \pm 0.06$	$0 \pm 0$	$0 \pm 0$	$0 \pm 10$
			MLT sectors			
NCF, FAC (noon)	$0.59 \pm 0.06$	$0.73 \pm 0.07$	$0.71 \pm 0.07$	$40 \pm 10$	$50 \pm 10$	$60 \pm 20$
NCF, FAC (dawn)	$0.70 \pm 0.06$	$0.82 \pm 0.05$	$0.86 \pm 0.04$	$35 \pm 5$	$30 \pm 10$	$50 \pm 10$
NCF, FAC (midnight)	$0.57 \pm 0.08$	$0.67 \pm 0.11$	$0.65 \pm 0.08$	$50 \pm 10$	$40 \pm 10$	$50 \pm 20$
NCF, FAC (dusk)	$0.64 \pm 0.08$	$0.81 \pm 0.05$	$0.82 \pm 0.07$	$30 \pm 10$	$40 \pm 10$	$50 \pm 10$

Note. The time lag is the time the second parameter lags behind the first one.

found for MC storms, then sheath storms and lowest values for HSS/SIR storms. The best lag between the driving function (NCF or  $\varepsilon$ ) and ionospheric quantities (FAC, SME/L/U) are 30–40 min for HSS/SIR and sheath storms, and 50–70 min for MC storms. The Polar Cap North (PCN) index (Troshichev et al., 1988) is an exception, showing a lag of only 20 min for HSS/SIR and sheath storms and 30 min for MC storms. This is consistent with the assumption that PCN is related to the cross-polar cap potential (Troshichev et al., 1996), which may respond more promptly to solar wind driving.

To study the ionospheric response to solar wind driving in different magnetic local time (MLT) sectors, best lag and corresponding CCs between the total FAC and NCF were calculated separately for the noon, dawn, midnight, and dusk sectors as shown in the bottom part of Table 1. Instead of the total downward FAC, the direction with the strongest FAC in each sector was used, that is, upward for dusk and midnight, and downward for noon and dawn. Separating the FAC into sectors makes the CCs slightly lower compared to the total hemispheric FAC in the upper part of Table 1. It is seen that the dawn and dusk sectors have the largest CCs for all interplanetary drivers. The shortest lags are found in HSS/SIR and sheath storms in the dawn and dusk sectors and are 30–40 min, while for MC storms the lags are 50–60 min at all MLT sectors. In the noon and midnight sectors, the lags are a bit longer, about 40–60 min.

Anderson et al. (2014) found that the dayside currents appear 20 min after the IMF southward turning and nightside currents after 60-90 min, thereafter the currents intensify at dawn, dusk, and dayside, yielding a fully developed R1/R2 current system after 30 min of nightside onset. McPherron et al. (2018) found that the dayside prediction filter rises rapidly from zero lag to a peak at  $\sim$ 40 min and the nightside response is delayed relative to the dayside peaking at  $\sim$ 60 min. Hence, the lags found here are of the same magnitude as those found in the previous studies. We do not find the shortest lags on the dayside, as Anderson et al. (2014) and McPherron et al. (2018), but on the other hand, they did not analyze dawn and dusk separately as we do. It should also be noted that we study the integrated FAC, and therefore smaller localized features are not visible. Localized and

PEDERSEN ET AL. 5 of 9

19448007, 2023, 11, Downloaded from https://agupubs.onlinelibrary.wiley.com/doi/10.1029/2023GL103151 by Johns Hopkins University, Wiley Online Library on [16/06/2023]. See the Terms and Cond

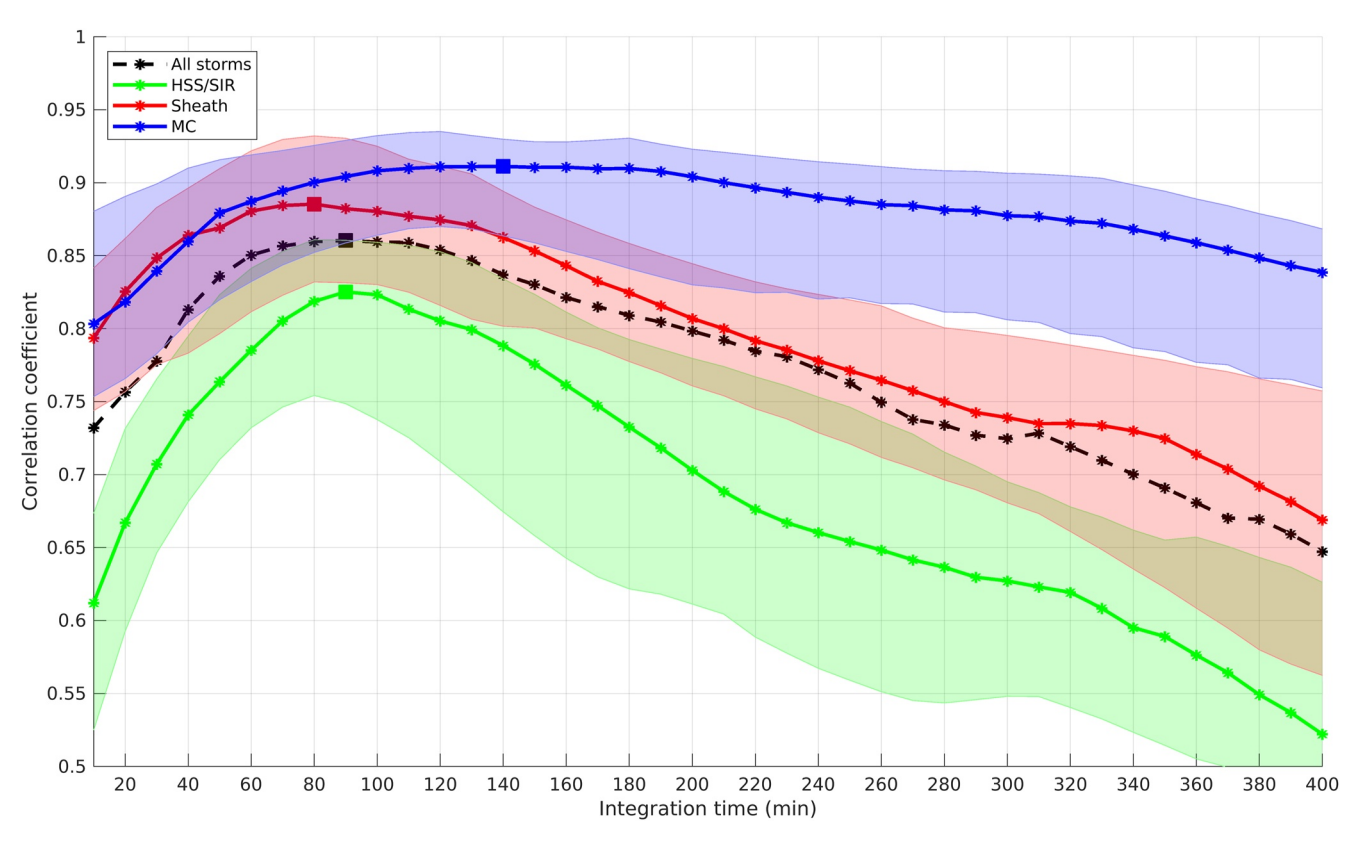


**Figure 3.** Correlation coefficient between field-aligned current and Newell coupling function (NCF) for different NCF integration times. The dashed black line shows the median correlation for all storms, solid line shows the median correlation in each storm category, the shaded area shows the span between the 25th and 75th percentiles for each storm category and the solid squares show the maxima.

transient features in the FAC and ionospheric currents have been observed on the dayside as a response to interplanetary shocks on shorter time scales (e.g., Oliveira & Raeder, 2014; Shi et al., 2022).

#### 3.3. Solar Wind Coupling Integration Time

Magnetosphere-ionosphere coupling can be directly driven by the solar wind, but it may also contain an indirectly driven component such as loading-unloading processes in the magnetosphere (Rostoker et al., 1988). This leads to the currents at any moment being affected by solar wind over an earlier time interval, which is likely to be longer than the 10 min used in the previous sections (see e.g., Newell et al., 2007). Therefore, the next step is to investigate, which is the NCF integration time yielding the maximum CC with the FAC. For brevity, it is called the best integration time in the following discussion. When increasing the integration time, we start from the time of the measured FAC and include solar wind data hitting the magnetopause at earlier times.

Figure 3 shows the CC between the total FAC and NCF for the NCF averaged over different preceding time windows. The solid lines show the median CC in each category and the shaded area values between the 25th and 75th percentiles. The CCs increase with increasing integration times up to 80 min for all drivers. This is in agreement with Laundal et al. (2018) who found that the CC between the coupling function and the AL and AU indices increased monotonically up to 60 min integration time of the coupling function, which was their upper limit. Here the largest CCs are reached at NCF integration time of 80 min for sheath storms, 90 min for HSS/SIR storms and 140 min for MC storms. If all drivers are analyzed together, the maximum correlation is observed at integration time of 90 min. Thus, by integrating the NCF, we get higher cross-correlation with FAC than by simply calculating lags (Table 1). The shape of the peak is sharpest for HSS/SIR, where CC values larger than 95% of the peak value can be found for integration times in the range 60–140 min. For sheath storms, integration times in range 30–160 min yield 95% of the peak CC, while for MC storms the range is 50–340 min. The larger

PEDERSEN ET AL. 6 of 9

range of integration times for sheath and particularly MC storms compared to HSS/SIR are consistent with the ACFs seen in Figure 1, with the solar wind/IMF typically having wider FWHMs for sheath and MC than for HSS/SIR storms.

#### 3.4. FAC by Different Drivers During Storm Main Phase

The relationship between the FAC and the NCF, the SME index, and the SYM-H index was investigated for the three storm drivers. Since the best integration times of the NCF found in Section 3.3 resulted in slightly higher CCs with FACs than the 10-min resolution NCF with best lags from Table 1, in this section the NCF integration times of 90, 80, and 140 min are used for HSS/SIR, sheath and MC storms, respectively. If more than 50% of the solar wind data are missing, those values are excluded. Figure 4 shows the distribution and linear fits between the FAC and NCF (top panels), FAC and SME index (middle panels), and FAC and -SYM-H index (bottom panels). Only data during the storm main phase are used.

From the distribution of FACs versus NCF seen in the top row of Figure 4, both the largest FACs and NCFs are observed during sheath-driven storms, with maximum FAC at 23.3 MA and NCF at  $52.3 \times 10^3$ . The spread in FAC values is largest for sheath-driven storms, as is evident from the 95% confidence limit (red lines). The same characteristics hold also for the SME-FAC and SYM-H-FAC relationships (middle and bottom rows). For the NCF-FAC plot, the HSS/SIR storms have the steepest slope and the smallest intercept, while sheath storms have the smallest slope and highest intercept. MC storms do not have small NCF nor FAC values. Sheath storm main phases contain cases with 2–3 MA FAC following almost zero integrated NCF. This could indicate that energy storage and sustained ring current play a role for these storms. The  $R^2$  parameter shows that the linear model is better for the NCF-FAC relationship in the case of the HSS/SIR storms ( $R^2 = 0.717$ ) than for sheath ( $R^2 = 0.589$ ) and MC ( $R^2 = 0.513$ ) storms.

The middle row shows the integrated FAC versus SME index. Based on the  $R^2$  values, the FAC is better predicted by the SME index in both the ICME sheath- and MC-driven storms than by the NCF. Interestingly, in the HSS/SIR-driven storms the FAC is better captured by the NCF than the SME index. This is somewhat surprising, considering the close connection between the FAC and horizontal currents affecting the SME index.

The relationship between the FAC and -SYM-H index is displayed in the bottom panels. Even though the  $R^2$  values are lower, many features (behavior of slopes and confidence intervals) between the storm types are similar to the top and middle panels. The low  $R^2$  values between the 10-min SYM-H index and FAC values shown in Figure 4 are in line with earlier observations. Pedersen et al. (2021, 2022) show that the largest FAC occurs early in the storm main phase for HSS/SIR and sheath storms, and a few hours before SYM-H minimum for MC storms.

#### 4. Conclusions

We have performed autocorrelation and cross-correlation analysis for the NCF, hemispherically integrated FAC, and several other parameters for storms driven by HSS/SIR, sheath, and MC.

The main findings are:

- ACFs of NCF are the widest for MC storms, then sheath, and narrowest for HSS/SIR storms. Same kind of behavior can be found for the total FAC and the SME index for these three types of storms.
- Using 10-min NCF data, the best lags are  $40 \pm 10$  min for HSS/SIR and sheath-driven storms, and  $60 \pm 10$  min for MC-driven storms, which result in CCs of 0.71, 0.84, and 0.87, respectively.
- For the total FAC, the dawn and dusk sectors have the highest correlations and shortest lags for all storm drivers.
- The integration time of the NCF yielding the highest CC with the total FAC is 90 min (60–140 min for CC greater than 95% of the peak value) for HSS/SIR, 80 min (30–160 min) for sheaths, and 140 min (50–340 min) for MC driven storms. The corresponding peak CCs are 0.83, 0.89, and 0.91, respectively.
- Integration of the NCF gives higher cross-correlation with FAC than by using lags at 10 min resolution.
- During the storm main phase, sheath-driven storms have the largest values and widest range of values for the total FAC, SME index, and NCF, while MC-driven storms have the narrowest range in values.

PEDERSEN ET AL. 7 of 9

19448007, 2023, 11, Downloaded from https://agupubs.onlinelibrary.wiley.com/doi/10.1029/2023GL103151 by Johns Hopkins University, Wiley Online Library on [16/06/2023]. See the Terms and Conditions (https://

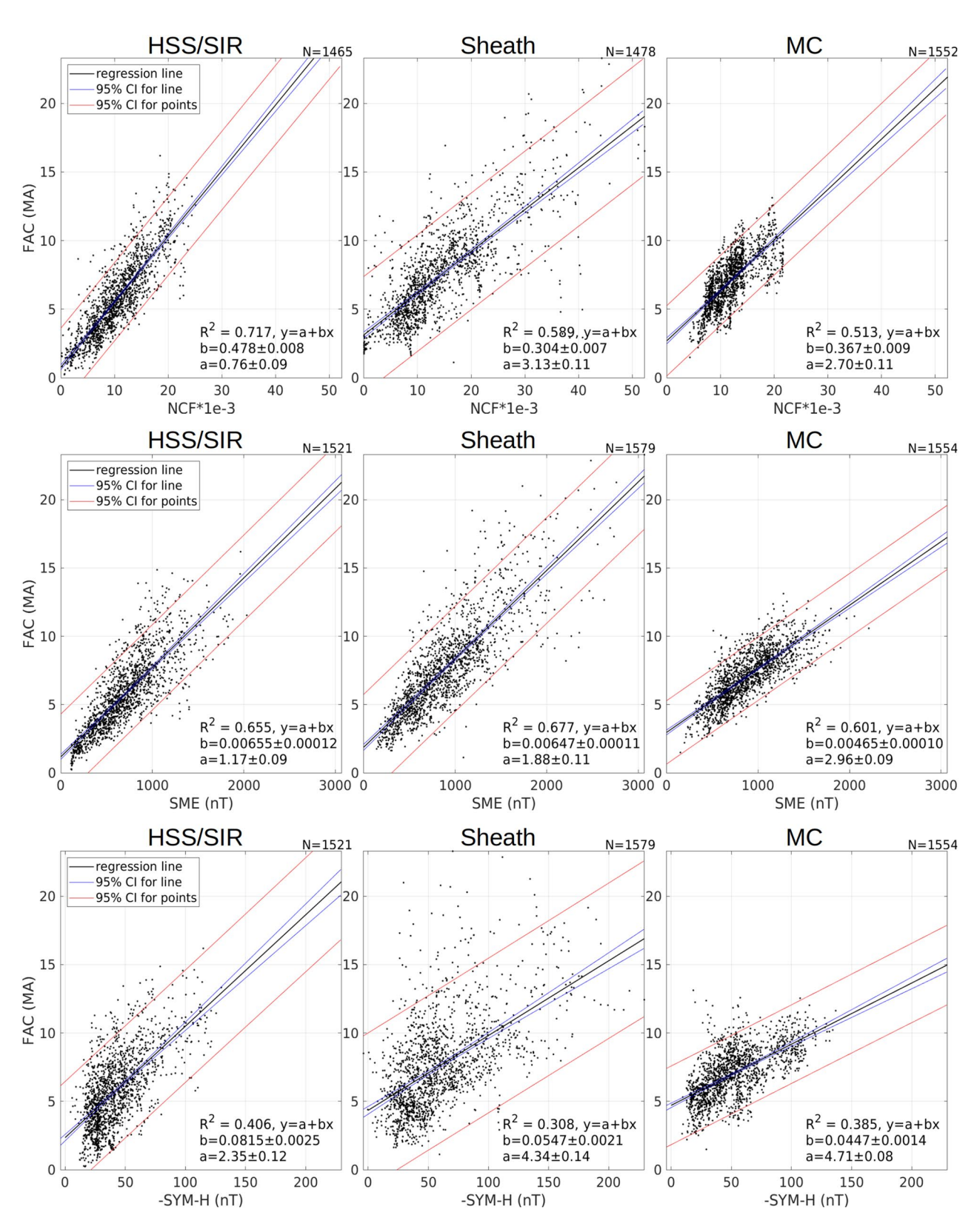


**Figure 4.** Total field-aligned current (FAC) and integrated Newell coupling function (top row), FAC and SME index (middle row) and FAC and -SYM-H index (bottom row) during the storm main phase for HSS/SIR (left column), sheath (middle column) and magnetic cloud (right column) driven storms. The solid black line shows the linear fit, the two blue lines show the 95% confidence interval of the linear fit line and the two red lines show the 95% confidence interval for the predicted FAC values. *N* is the number of data points included in each panel.

PEDERSEN ET AL. 8 of 9

19448007, 2023, 11, Downlo

om/doi/10.1029/2023GL103151 by Johns

Surprisingly, when a linear fit is carried out, the total FAC during the main phase of HSS/SIR storms is better
predicted by the integrated NCF than the SME index.

#### **Data Availability Statement**

A list of all geomagnetic storms included in this study is attached as Supporting Information S1. The fitted field-aligned current data from AMPERE is available at https://ampere.jhuapl.edu/download/. The horizontal ionospheric equivalent currents and SME/U/L indices from SuperMAG are available through https://supermag.jhuapl.edu/info/. The geomagnetic indices, solar wind and interplanetary field data from OMNIWeb can be downloaded from https://omniweb.gsfc.nasa.gov/form/omni\_min\_def.html.

#### Acknowledgments References

This work was supported by the Academy of Finland projects 314664 and 348782, and the Vilho, Yrjö and Kalle Väisälä Foundation. We thank the AMPERE team and the AMPERE Science Center for providing the Iridium derived data products. For the SME indices we gratefully thank the SuperMAG collaboration and all organizations involved (https://supermag.jhuapl.edu/info/). For the geomagnetic indices, solar wind and interplanetary magnetic field data we gratefully thank NASA/GSFC's Space Physics Data Facility's OMNIWeb (https://omniweb.gsfc.nasa.gov/).

- Anderson, B., Korth, H., Waters, C., Green, D., Merkin, V., Barnes, R., & Dyrud, L. (2014). Development of large-scale Birkeland currents determined from the Active Magnetosphere and Planetary Electrodynamics Response Experiment. Geophysical Research Letters, 41(9), 3017–3025. https://doi.org/10.1002/2014gl059941
- Anderson, B., Takahashi, K., Kamei, T., Waters, C., & Toth, B. (2002). Birkeland current system key parameters derived from iridium observations: Method and initial validation results. *Journal of Geophysical Research*, 107(A6), SMP-11. https://doi.org/10.1029/2001JA000080 Anderson, B., Takahashi, K., & Toth, B. A. (2000). Sensing global Birkeland currents with Iridium® engineering magnetometer data. *Geophysical Research Letters*, 27(24), 4045–4048. https://doi.org/10.1029/2000gl000094
- Belcher, J., & Davis, L., Jr. (1971). Large-amplitude Alfvén waves in the interplanetary medium, 2. *Journal of Geophysical Research*, 76(16), 3534–3563. https://doi.org/10.1029/JA076i016p03534
- Echer, E., Tsurutani, B., Gonzalez, W., & Kozyra, J. (2011). High speed stream properties and related geomagnetic activity during the whole heliosphere interval (WHI): 20 March to 16 April 2008. Solar Physics, 274(1), 303–320. https://doi.org/10.1007/s11207-011-9739-0
- Gonzalez, W. D., Tsurutani, B. T., Gonzalez, A. L., Smith, E. J., Tang, F., & Akasofu, S.-I. (1989). Solar wind-magnetosphere coupling during intense magnetic storms (1978–1979). *Journal of Geophysical Research*, 94(A7), 8835–8851. https://doi.org/10.1029/JA094iA07p08835
- Laundal, K. M., Finlay, C. C., Olsen, N., & Reistad, J. P. (2018). Solar wind and seasonal influence on ionospheric currents from swarm and champ measurements. *Journal of Geophysical Research: Space Physics*, 123(5), 4402–4429. https://doi.org/10.1029/2018JA025387
- Maggiolo, R., Hamrin, M., De Keyser, J., Pitkänen, T., Cessateur, G., Gunell, H., & Maes, L. (2017). The delayed time response of geomagnetic
- activity to the solar wind. *Journal of Geophysical Research: Space Physics, 122*(11), 11–109. https://doi.org/10.1002/2016JA023793

  McPherron, R., Anderson, B., & Chu, X. (2018). Relation of field-aligned currents measured by the network of Iridium® spacecraft to solar wind
- and substorms. *Geophysical Research Letters*, 45(5), 2151–2158. https://doi.org/10.1002/2017GL076741

  Meng, C.-I., Tsurutani, B., Kawasaki, K., & Akasofu, S.-I. (1973). Cross-correlation analysis of the *AE* index and the interplanetary magnetic
- field  $B_Z$  component. Journal of Geophysical Research, 78(4), 617–629. https://doi.org/10.1029/JA078i004p00617 Newell, P., Sotirelis, T., Liou, K., Meng, C.-I., & Rich, F. (2007). A nearly universal solar wind-magnetosphere coupling function inferred from
- 10 magnetospheric state variables. *Journal of Geophysical Research*, 112(A1). https://doi.org/10.1029/2006JA012015
  Oliveira, D. M., & Raeder, J. (2014). Impact angle control of interplanetary shock geoeffectiveness. *Journal of Geophysical Research: Space*
- Physics, 119(10), 8188–8201. https://doi.org/10.1002/2014JA020275

  Pedersen, M., Vanhamäki, H., Aikio, A., Waters, C., Gjerloev, J., Käki, S., & Workayehu, A. (2022). Effect of ICME-driven storms on field-aligned
- Pedersen, M., Vanhamaki, H., Aikio, A., Waters, C., Gjerloev, J., Kaki, S., & Workayehu, A. (2022). Effect of ICME-driven storms on field-aligned and ionospheric currents from AMPERE and SuperMAG. *Journal of Geophysical Research: Space Physics*, 127(8), e2022JA030423. https://doi.org/10.1029/2022JA030423
- Pedersen, M., Vanhamäki, H., Aikio, A. T., Käki, S., Workayehu, A. B., Waters, C. L., & Gjerloev, J. W. (2021). Field-aligned and ionospheric currents by AMPERE and SuperMAG during HSS/SIR-driven storms. *Journal of Geophysical Research: Space Physics*, 126(11), e2021JA029437. https://doi.org/10.1029/2021JA029437
- Rostoker, G., Akasofu, S., Baumjohann, W., Kamide, Y., & McPherron, R. (1988). The roles of direct input of energy from the solar wind and unloading of stored magnetotail energy in driving magnetospheric substorms. *Space Science Reviews*, 46(1), 93–111. https://doi.org/10.1007/BF00173876
- Rostoker, G., Lam, H.-L., & Hume, W. D. (1972). Response time of the magnetosphere to the interplanetary electric field. *Canadian Journal of Physics*, 50(6), 544–547. https://doi.org/10.1139/p72-073
- Shi, X., Lin, D., Wang, W., Baker, J. B., Weygand, J. M., Hartinger, M. D., et al. (2022). Geospace concussion: Global reversal of ionospheric vertical plasma drift in response to a sudden commencement. *Geophysical Research Letters*, 49(19), e2022GL100014. https://doi.org/10.1029/2022GL100014
- Troshichev, O., Andrezen, V., Vennerstrøm, S., & Friis-Christensen, E. (1988). Magnetic activity in the polar cap—A new index. *Planetary and Space Science*, 36(11), 1095–1102. https://doi.org/10.1016/0032-0633(88)90063-3
- Troshichev, O., Hayakawa, H., Matsuoka, A., Mukai, T., & Tsuruda, K. (1996). Cross polar cap diameter and voltage as a function of PC index and interplanetary quantities. Journal of Geophysical Research, 101(A6), 13429–13435. https://doi.org/10.1029/95JA03672
- Tsurutani, B. T., & Gonzalez, W. D. (1987). The cause of high-intensity long-duration continuous AE activity (HILDCAAS): Interplanetary Alfvén wave trains. Planetary and Space Science, 35(4), 405–412. https://doi.org/10.1016/0032-0633(87)90097-3
- Tsurutani, B. T., Gonzalez, W. D., Gonzalez, A. L., Guarnieri, F. L., Gopalswamy, N., Grande, M., et al. (2006). Corotating solar wind streams and recurrent geomagnetic activity: A review. *Journal of Geophysical Research*, 111(A7), A07S01. https://doi.org/10.1029/2005JA011273
- Tsurutani, B. T., & Ho, C. M. (1999). A review of discontinuities and Alfvén waves in interplanetary space: Ulysses results. *Reviews of Geophysics*, 37(4), 517–541. https://doi.org/10.1029/1999RG900010
- Waters, C., Anderson, B., Green, D. L., Korth, H., Barnes, R. J., & Vanhamäki, H. (2020). Science data products for ampere. In M. W. Dunlop & H. Lühr (Eds.), Ionospheric multi-spacecraft analysis tools: Approaches for deriving ionospheric parameters (pp. 141–165). Springer International Publishing. https://doi.org/10.1007/978-3-030-26732-2\_7
- Waters, C., Anderson, B., & Liou, K. (2001). Estimation of global field aligned currents using the Iridium® system magnetometer data. *Geophysical Research Letters*, 28(11), 2165–2168. https://doi.org/10.1029/2000gl012725
- Wilcox, J. M., Schatten, K. H., & Ness, N. F. (1967). Influence of interplanetary magnetic field and plasma on geomagnetic activity during quiet-Sun conditions. *Journal of Geophysical Research*, 72(1), 19–26. https://doi.org/10.1029/JZ072i001p00019

PEDERSEN ET AL. 9 of 9